Title: Robotic Four-Dimensional Pixel Assembly of van der Waals Solids

Authors: Andrew J. Mannix[#1,+], Andrew Ye[#2], Suk Hyun Sung[3], Ariana Ray[4], Fauzia Mujid[6], Chibeom Park[6], Myungjae Lee,[1] Jong-Hoon Kang,[6] Robert Shreiner[7], Alexander A. High[2,8], David A. Muller[4,5] Robert Hovden[3], Jiwoong Park*[,1,2,6]

Affiliations:

[1]James Franck Institute, University of Chicago, Chicago, IL 60637, USA.

[2]Pritzker School of Molecular Engineering, University of Chicago, Chicago, IL 60637, USA.

[3]Department of Materials Science and Engineering, University of Michigan, Ann Arbor, USA.

[4]School of Applied and Engineering Physics, Cornell University, Ithaca, NY 14853, USA.

[5]Kavli Institute at Cornell for Nanoscale Science, Ithaca, New York 14853, USA.

[6]Department of Chemistry, University of Chicago, Chicago, IL 60637, USA.

[7]Department of Physics, University of Chicago, Chicago, IL 60637, USA.

[8]Center for Molecular Engineering and Materials Science Division, Argonne National Laboratory, Lemont, IL 60439, USA.

[#]Equal author contributions

*Corresponding Authors: Jiwoong Park. jwpark@uchicago.edu

[+]Current affiliation: Department of Materials Science and Engineering, Stanford University

Van der Waals (vdW) solids can be engineered with atomically-precise vertical composition through the assembly of layered 2D materials (2DMs)[1,2]. In doing so, the structure-defined interlayer interactions result in novel phenomena, including superconductivity[3–5], exciton bands[6–11], and 2D Hubbard physics[12–15]. Such phenomena have been observed in vdW heterostructures and moiré superlattices produced using an artisanal method[3,16] of assembling micromechanically-exfoliated flakes. However, further engineering and application of vdW solids requires a scalable and rapid production method to precisely design and control composition and structure over all three spatial dimensions (*x*, *y*, *z*) and interlayer rotation (*θ*). Here, we demonstrate such an approach, *Robotic 4D Pixel Assembly*, for rapidly manufacturing designer vdW solids with unprecedented speed, area, patternability, and angle control. We utilize the robotic assembly of prepatterned pixels made from atomically-thin 2DM components. Wafer-scale 2DM films are grown, patterned through a clean, contact-free process, and assembled together with engineered adhesive stamps actuated by a high vacuum robot. Our technique led to the fabrication of vdW solids of up to 80 individual layers, consisting of $(100\ \mu m)^2$ areas with pre-designed patterned shapes, laterally/vertically programmed composition, and controlled interlayer angle. Cryogenic spectroscopic benchmarks of the material quality are indistinguishable from manual stacking. Our manufactured structures enabled efficient optical spectroscopic assays of vdW solids, revealing new excitonic and absorbance layer dependencies in MoS_2. Furthermore, our approach allows for the fabrication of twisted *N*-layer assemblies, where we observe atomic reconstruction of twisted 4-layer WS_2 at unexpectedly high interlayer twist angles of ≥4°. Our vdW solids manufacturing enables rapid construction of atomically-resolved quantum materials and will help realize the full potential of vdW heterostructures as a platform for novel physics[2,5] and advanced electronic technologies[17,18].

Precise three-dimensional spatial control of the composition and structure of inorganic crystalline materials like silicon is the foundation for integrated circuitry. Van der Waals (vdW) solids generated by

stacking two-dimensional materials (2DMs) are not limited by lattice commensurability and interlayer bonding[1], providing two key advantages over the conventional production of sequentially deposited crystals. First, lattice and chemical flexibility between adjacent layers means that one can produce arbitrary vertical sequences of crystal compositions with layer-tunable electrical[3–5], magnetic[4,19], and optoelectronic[6,10–12] properties. Second, this interlayer flexibility introduces an additional dimension of θ, the interlayer lattice rotation or twist, as a new degree of freedom for controlling the properties of vdW solids. This has been seen in recent demonstrations of momentum-space crystal engineering and superconductivity of twisted bilayer[3–5,20] and trilayer[21] 2DMs. Such advantages are complementary to conventional methods of three-dimensional control via patterning and provide a powerful approach for producing solids whose properties can be systematically and precisely designed. Realizing these characteristics of a designer solid requires accurate placement of many 2DM *pixels* (i.e., discrete components, not necessarily square-shaped) onto target positions (x, y, z) with a specified interlayer angular orientation (θ) (Fig. 1a). A method that could achieve this would enable the production of 3D, monolithically integrated solids with parameters such as layer number (N), chemical composition, and crystalline structure that are programmatically dictated and controlled.

However, current 2DMs processing techniques provide only partial control (principally z and θ) with limited throughput. Conventional 2DMs vdW heterostructure assembly relies on the irregularly shaped mono- and multilayers isolated through micro-mechanical exfoliation[1]. While exfoliated materials maintain remarkable quality, their inherent stochastic distribution and small area do not permit the facile production of integrated solids. Emerging wafer-scale growth through chemical vapor deposition (CVD)[22,23] , metal-organic chemical vapor deposition (MOCVD)[24], controlled recrystallization[25], and solution-based techniques have brought us closer to vdW solid manufacturing, with electronic properties in the best cases rivaling those of exfoliated materials[22].

In this work, we present a versatile high throughput approach for producing designer vdW solids with a full four-dimensional control of x-y-z-θ, as illustrated in Fig. 1b. For this, we combine (i) wafer-

scale synthesis of various 2DMs with two further technical advances: (ii) a contact-free patterning technique to mass produce pixel building blocks from wafer-scale synthesized 2DMs and (iii) a high throughput, operator-free *Robotic 4D Pixel Assembly* manufacturing system to assemble these pixels under high vacuum. During the assembly step, multiple pixels, each pre-designed with a shape, are chosen and stacked with a precise spatial resolution (*x*-*y*), atomic scale layer control (*z* and *N*), and angle resolution (θ).

The versatility of our method enables the design and production of a variety of integrated vdW homo- and hetero-structures. Figure 1b (iii) illustrates four example structures: a multilayer vdW solid with a large *N*, an alternating (ABAB...) heterostructure with varying pixel sizes, an offset heterostructure with laterally displaced pixels, and an angle controlled spiral stack. We successfully produced these using our *Robotic 4D Pixel Assembly*, as shown in Fig. 1c. which displays the optical micrographs (from left to right) of a 25-layer stacked WS_2, an alternating 7-layer MoS_2/WS_2 superlattice with shrinking WS_2 pixels, an offset MoS_2/WSe_2 heterostructure with three smaller WSe_2 pixels diagonally aligned, and a 4-layer WS_2 "spiral staircase" with a constant interlayer $\theta = 12.5^o$. Our deterministic and consistent technique allows us to manufacture these structures at rates on the order of 30 layers/hour (Supplementary Table 1), significantly faster than the state-of-the-art for exfoliated materials[26]. At the same time, our technique preserves the quality of the starting material, as demonstrated by the narrow linewidths observed in cryogenic photoluminescence of exfoliated samples (Supplementary Fig. 1). In the following text, we explain our method in more detail and present two applications realized using designer vdW solids we generated using polycrystalline monolayers (Fig. 1-3) and single crystalline ones (Fig. 4).

The core fixture of our *Robotic 4D Pixel Assembly* process is our vacuum assembly robot (VAR, Fig. 2a, Supplementary Fig. 2). It consists of a heated *x*-*y* translation stage that holds multiple ~1 cm^2 chips of source material or receiving substrates, and a separate *z*-θ actuated stacking platform which moves a microstructured polymer stamp (Fig. 2b) for picking up 2DMs to form the stack. The VAR is housed within a desktop-size high vacuum chamber ($P_{base} \sim 10^{-6}$ Torr) to reduce surface contamination,

prevent material oxidation, and promote high quality interfaces during assembly. An external optical microscope and digital camera aimed through the top viewport provides lateral alignment and process monitoring, including the detection of stamp/substrate contact to prevent excessive force (Supplementary Fig. 3). The manufacturing process in the VAR (Fig. 2c) consists of two sequential phases:

(i) During assembly, the VAR loops through a process cycle of (1) navigating the stamp to the selected pixel for pick-up, (2) placing the stamp into contact, and (3) lifting to pick up the target layer, which is now added to the stacked vdW solid. This process repeats to add additional layers to the stack on the stamp.

(ii) The terminal deposition step involves (1) navigating the stamp to a desired location on the target substrate, (2) contacting the target point with applied release stimulus, typically heat, and (3) releasing the assembled vdW solid by slowly lifting the *z*-stage.

A multilayer polymer stamp (Fig. 2b) plays a key role during these two phases. It is specifically designed to exhibit optimized mechanical properties and thermally switched adhesion determined by the glass transition temperature[27], thermolytic release layer decomposition[28], and viscoelastic relaxation[29]. Details of the VAR assembly process, operational parameters, and stamp fabrication are given in the Methods and Supplementary Information. The VAR assembly works for TMDs, Au thin films (Supplementary Fig. 5), exfoliated flakes of graphite, hBN (Supplementary Fig. 6), and WSe_2 (Supplementary Fig. 1), and is expected to apply to the variety of materials compatible with vdW stacking[17,30–33]. Furthermore, the VAR can be used to produce high quality vdW heterostructures from exfoliated flakes, such as hBN-encapsulated WSe_2, which shows narrow linewidth cryogenic photoluminescence spectra similar to those from manually stacked samples (Supplementary Fig. 1).

This manufacturing process is computer controlled and the full process, from pick-up of the first layer to transfer of the completed vdW solid, can be fully automated to take advantage of wafer-scale synthetic monolayers. Examples of an automated recipe-driven process are shown in Fig. 3c and

Supplementary Video 1. One immediate advantage of automation is its high throughput. This is highlighted by the operator-free fabrication of the 80 layer MoS_2 (Supplementary Fig. 7). Assembly of such structures through traditional manual or semi-automated methods would be tedious and challenging.

The other key technical advance is the fabrication of patterned 2DM building blocks (Fig. 1b (ii)) through a clean, non-perturbative lithographic technique. Conventional photo- or electron beam lithography processes involve contact with polymers, chemical developers, and solvents, which contaminate vdW interfaces[34,35]. Instead, we used template-strip lithography (TSL), an adhesion-based[27,36], dry patterning technique for 2DMs (schematic shown in Fig. 2d) that prevents deposition of surface residues by not touching the pixel region with the patterning medium. It uses a microstructured template with patterned adhesive regions produced via standard cleanroom lithography; these adhesive regions stick to the 2DM areas, which are then cleaved and stripped away when the template is lifted from the surface leaving the non-contacted 2DM regions behind to generate patterned arrays of 2D pixels. Optical images of an example array made from monolayer WS_2 are shown in Fig. 2e, and an MoS_2 array as Supplementary Fig. 8, which show a high yield of 99%. AFM and optical microscopy are used to confirm clean surfaces with no polymer residues after patterning (Supplementary Figs. 8 and 9).

The precise grid spacing within each patterned chip facilitates the calculation of the spatial coordinates of every pixel (Fig. 2e and Supplementary Fig. 8). It is therefore no longer necessary to individually search, locate, catalog, and characterize the thickness of stochastically exfoliated materials; we can pre-design the structure of the incorporated layers. With this deterministic material source as input, the VAR software can interpret scripted recipes of coordinates and stacking conditions to sequentially pick up pixels and manufacture a programmed vdW solid. Spatially resolved measurements including laser confocal microscopy (Supplementary Fig. 10) and Raman spectroscopic mapping (Supplementary Fig. 11) confirm the uniformity of our assembled samples. Moreover, mm-scale stamps enable larger heterostructures and parallel batch assembly of multiple structures (Supplementary Fig. 12). These qualities differentiate our *Robotic 4D Pixel Assembly* process from conventional exfoliated 2DM

stacking. We design and conduct two such experiments realized using custom-produced vdW solids: comprehensive optical assay of *N*-layer stacked MoS_2 (Fig. 3) and structural characterization of angle-controlled 4-layer WS_2 (Fig. 4).

Figure 3 describes the first example – a MoS_2 solid (100 by 100 μm) that consists of 16 square regions, each with a different *N* ranging from 1 to 16 (see optical image, Fig. 3a). This 16-tile configuration is specifically designed for one-shot characterization of the *N*-dependent evolution of the properties of polycrystalline 2DMs, where every interlayer interface has random interlayer rotation. Such information cannot be easily obtained from other samples such as randomly sized exfoliated flakes[37,38] or multiple samples with statistical thickness fluctuations produced via thin-film growth[39,40]. This structure is a stack of 16 Tetris-like pixels (Fig. 3b), and each pixel is specifically patterned and assembled layer-by-layer (see Fig. 3c for the images during assembly, and Supplementary Video 1) according to the overall design of the solid. The 16-tile solid in this case has been deposited onto a uniform MoS_2 substrate layer to yield 1-17 layers (where monolayer properties can be probed outside the tiled region). The high quality of interlayer interfaces are confirmed by cross-sectional scanning transmission electron microscopy (STEM) images (Fig. 3d) taken from different regions (thus different *N*'s) of another similarly produced sample.

Using hyperspectral microscopy, we measure the transmission (*T*) and reflection (*R*) images of this solid at different wavelengths λ (after the sample is transferred to a sapphire substrate). Example images (λ = 680 nm) are shown in Fig. 3e, which shows uniform contrast in each tile region. By comparing these images with substrate and mirror reference images, we measure the reflection ($R(\lambda, N)$) and absorption ($A(\lambda, N) = 1 - T - R$) spectra of the 16-tile optical-assay, each averaged over one tile region. The resulting absorption spectra for N = 1 - 17 are shown in Fig. 3f and display a layer-dependent evolution of the peak positions and magnitude. First, despite the random interlayer orientations present in our samples, these spectra show two clearly resolved absorption peaks near the *A*- and *B*-exciton energies. The fitted peak positions (Fig. 3g) for smaller *N* are close to the values previously observed in mono- and

bilayer-MoS_2[41], and they then decrease and converge near the values of bulk 2H-MoS_2[42]. This suggests that the intralayer direct-gap K-K (or K'-K') transition, which is insensitive to interlayer rotations, remains dominant in our stacked MoS_2 solid. Second, this also suggests that the magnitude of $R(\lambda, N)$ and $A(\lambda, N)$ of stacked MoS_2 can be understood for different N using a simple model without explicitly considering the interlayer rotation angles. We find that this is indeed the case: the absorption spectra in Fig. 3f can be closely matched for all N using a simple transfer matrix method (TMM)[43] calculation based on monolayer optical constants as the building blocks (Supplementary Fig. 12). Such insensitivity of R and A to the interlayer rotations has practical implications, as it allows for modeling stacked MoS_2 films as a single material for photonic applications. Another finding is that the reflectance R converges to the 3D-bulk-crystal limit quickly for thin MoS_2 films: even at $N = 17$ (thickness ~ 10 nm), the stacked film reflects approximately ~ 40% of incoming light on average (Supplementary Fig. 12), close to the reflectivity of bulk MoS_2.

Photoluminescence (PL) taken from the 16-tile optical-assay (Fig. 3g, 3h) also shows N-dependent evolution. There is an 87% decrease in the integrated intensity of the main A-exciton peak from 1L to 2L (Supplementary Fig. 13), which is comparable to other stacked bilayer samples[44,45] and explained by direct-to-indirect gap transition. However, when compared to natural 2H-MoS_2 at thicknesses greater than 2L, our assay shows less PL quenching with increasing N and a broadening of the direct A-exciton transition peak[46]. Both observations may result from the modified interlayer hybridization present in the rotationally misaligned layers and multiple domains contributing to the observed signal. Finally, we note that we observe one N-dependent effect in all our measured spectra (R, A, and PL). As N is increased from 1 to ~5, gradual red-shifts of both A- and B-exciton peaks are observed, which occurs due to enhanced screening[47–49].

Figure 4 presents our second demonstration – a multilayer WS_2 solid with precise interlayer rotations. It showcases the angle control of our robotic stacking system. This is an important new capability for designing 2DM-based solids with strongly correlated electronic and excitonic states[2,5].

Figure 4a shows selected area electron diffraction (SAED) for a 4-layer WS_2 sample, obtained by our nanomanufacturing technique using large (~ 100 μm) single-crystal WS_2 grown via MOCVD (inset) as the source. The single crystallinity of this source material is discussed further in Supplementary Fig. 14. Different regions of the triangle were picked up using our stamps, piece-by-piece, with interlayer rotation applied between each layer. This allows us to generate multilayer twisted heterostructures, with every interlayer rotation angle controlled. This method can be generally applied to form more complex stacks using larger single-crystalline[50] or lattice oriented[51] 2DM sources.

The diffraction pattern in Fig. 4a clearly shows 4 sets of primary Bragg peaks, each rotated slightly from the neighboring ones. All three interlayer twist angles (θ_{12}, θ_{23}, θ_{34}) are close to 4.2° (mean of 4.2° ± 0.2) with θ_{12} being larger than the other two. The precision of the rotation angle realized in our stack is currently limited by the open-loop mechanical resolution of our angle actuator (± 0.2°, Supplementary Fig. 15), although there could be additional contributions from unintentional movement of each 2DM piece induced during and after the pick-up and small orientation variation within the single crystal source materials.

Surprisingly, we observe strong satellite peaks beyond the primary Bragg peaks, as shown by the magnified images (Fig. 4b i-iii). Figure 4c further shows a dark-field TEM image obtained by selecting the 2nd order Bragg peaks and surrounding satellites (set ii, green box). Larger "fishnet" domains separated by dark boundaries are clearly visible in these images, with their spatial period (of the order of 10 nm) corresponding to the moiré wavelength for $\theta \approx 4°$. Multislice simulation of a rigid 4-layer WS_2 4.2° rotated structure (Supplementary Fig. 16) indicates that satellite peaks arising from multiple-scattering would have a nearly undetectable signal, therefore the apparent satellite peaks in Fig. 4a,b must be evidence of atomic reconstruction[52,53]. Our measured ratio between main Bragg peak to primary satellite peak is 1-2% (Supplementary Fig. 17), nearly twice of what would be expected from rigid lattice multiple scattering. We also observe in Fig. 4c the superimposed striped pattern. This corresponds to the moiré wavelength of the outer two layers, $3\theta \approx 12°$. Together, the fishnet and striping domains indicate

that it is likely that the inner two layers are restructuring. However, it is yet unclear whether the reconstruction occurs solely from the interactions between the interior two layers, or whether there are cooperative multilayer interactions. Future work will seek to elucidate the nature of such *N*-layer twisted interactions.

Our observation of lattice restructuring at $\theta \approx 4.2°$ is unexpected. The lattice reconstruction is driven by a reduction in interfacial energy, which is proportional to the size of the reconstructed domain. As the domain size is inversely proportional to twist angle, reconstruction due to interlayer interactions was previously observed at smaller twist angles (e.g., up to ~3° for graphene[52], ~2° for TMDCs[53]). However, modified interlayer mechanical coupling[54] and strongly correlated states[20] have been observed at twist angles up to ~5° in bilayer TMDCs, underscoring the importance of understanding atomic reconstruction in these materials. Moreover, atomic-scale engineered chirality[55] applied to 2D semiconductors may potentially enable efficient photonic and quantum information processing by enhance the coupling between light helicity and valley polarization[56] or enhanced non-linear optical phenomena[57].

Robotic 4D Pixel Assembly presents a new method for manufacturing precise vdW solids, highlighted by our two demonstrations of one-shot optical assays and twisted multilayer stacking. Some limitations of the VAR, namely lateral and angular resolution, could be improved by using higher specification closed-loop actuators. The lateral size of the assembled area can be increased by developing a larger stamp that can make contact with optimal and uniform force (See Supplementary Fig. 19). Strain formation, especially at high layer counts, could be reduced by minimizing unconstrained thermomechanical stresses on the 2D-polymer interface (See supplementary discussion). Our large sample size and predominantly monolayer source material are challenging compared to the common practice of using a thicker flake of hBN as the top layer, which acts as a mechanical buffer layer and decouples the heterostructure from slight mechanical deformation imparted by the polymeric stamp. Contrasting with existing fabrication methods based on exfoliated materials (where each device is

unique), our manufacturing process could enable efficient assembly of identical structures on the same chip. When combined with the growth of large single crystals of 2DMs, our assembly technique could enable high-throughput investigation of engineered electronic states in more complex, multilayer twisted heterostructures[21,58,59]. This also establishes an avenue for harnessing twisted structures in technological applications. Moreover, beyond wafer-scale synthesized TMDs, the processes of large area material synthesis, precise patterning, and automated assembly should generalize to other categories of delaminable materials, such as thin film electrodes[30,31], 2D complex oxides[32,60] or molecular monolayers[33].

Figures:

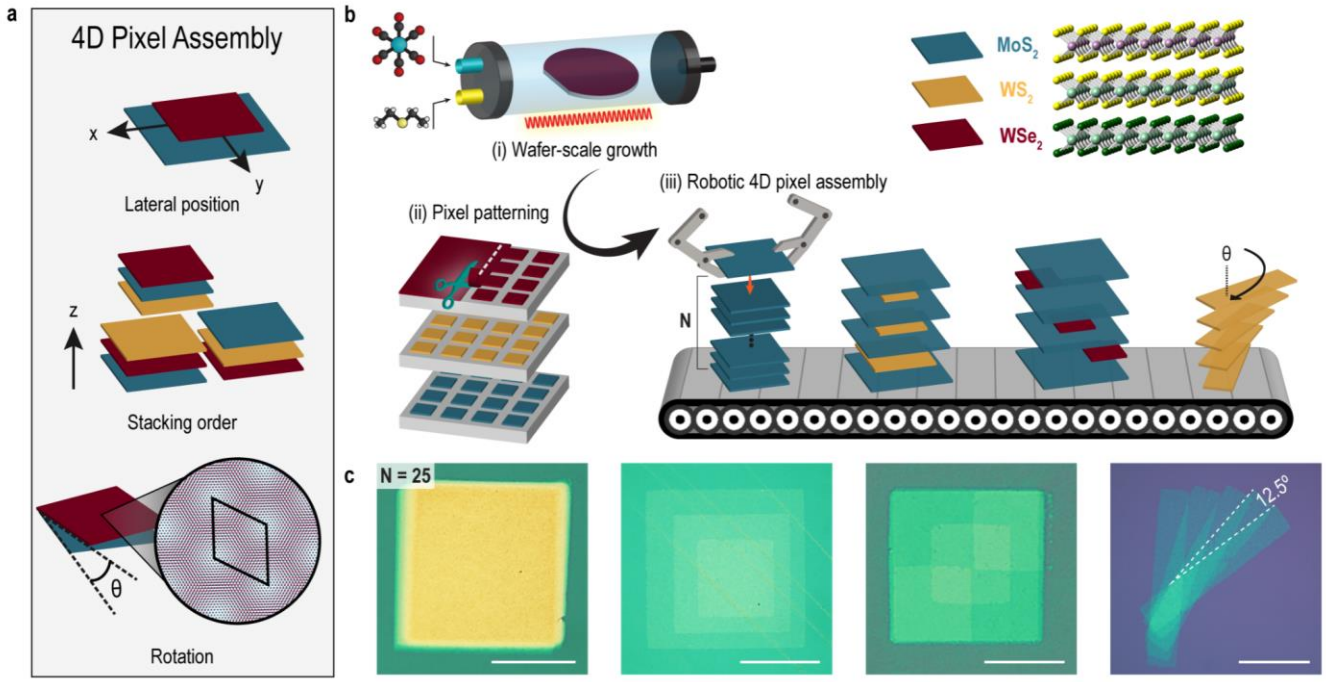

Figure 1. Robotic 4D Pixel Assembly. a, 4D pixel assembly concept diagram. **b**, Production of pixels by (i) wafer-scale growth and (ii) pixel patterning and automated pixel assembly by a robotic instrument (iii). **c**, Corresponding micrographs of vacuum assembly robot-manufactured vdW solids demonstrating layer number, composition, lateral position, and interlayer twist angle control (all scale bars 50 μm).

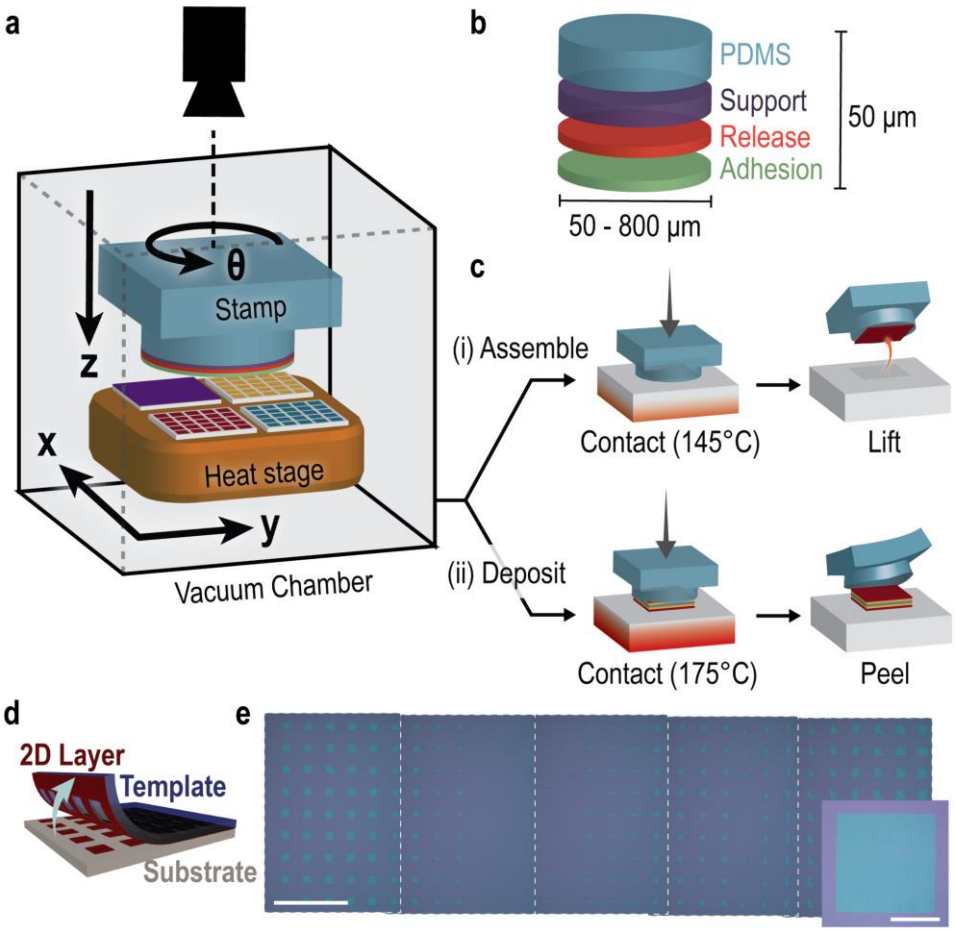

Figure 2. Automated vacuum assembly of van der Waals heterostructures. a, Diagram of Vacuum Assembly Robot (VAR) for vdW heterostructure fabrication. **b**, Schematic of adhesive stamp structure, where the multilayer structure mediates programmed adhesion and deposition via thermal and/or UV light activation of the release layer to generate rapid decomposition. Details of stamp polymers are included in Methods. **c**, Process flow chart demonstrating steps for (i) assembly of heterostructures and (ii) deposition of heterostructures onto a receiving substrate. **d**, Schematic of template strip lithography (TSL) process. **e**, Stitched optical micrographs from 13x13 mm^2 chip of square, rectangle, triangle, and tiled WS_2 pixels produced by TSL, scale bar 1 mm. Inset**:** Optical micrograph of an individual square pixel (scale bar 50 µm).

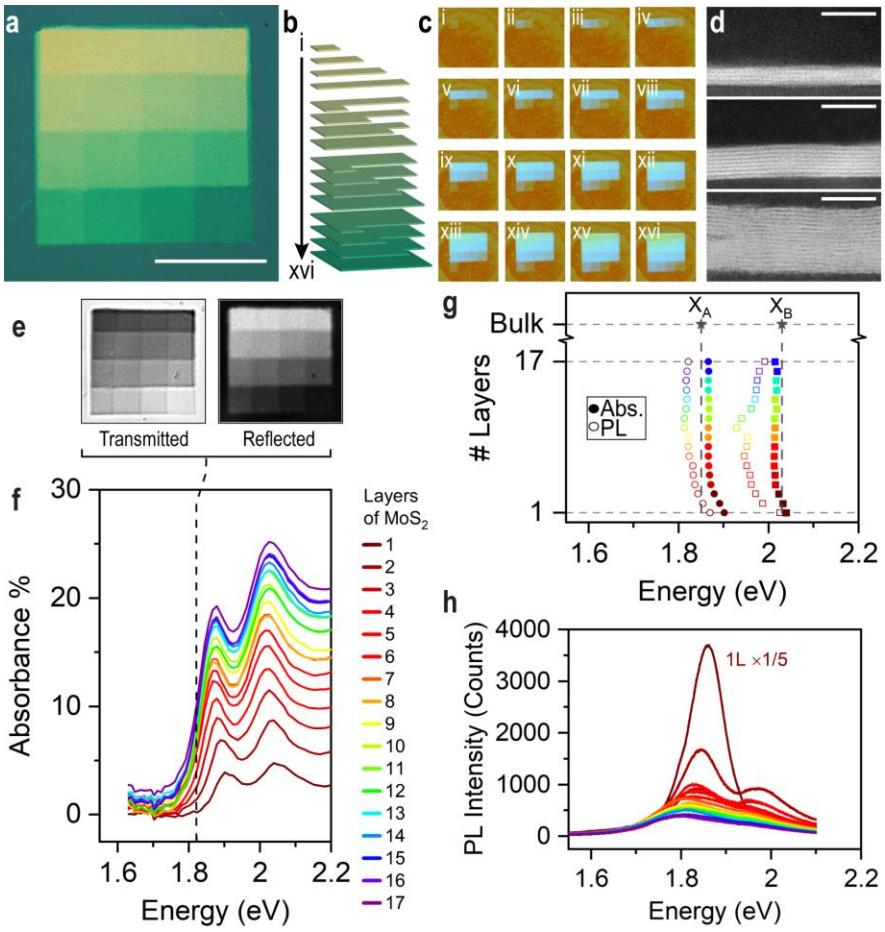

Figure 3. Comprehensive optical assay of *N*-layer stacked MoS_2. a, White light optical micrograph of 1 – 16L MoS_2 grid structure (scale bar 50 μm). **b**, Schematic of structured pixel assembly to realize 16-tile grid structure. **c**, In situ micrographs of designed heterostructure fabrication, where images were taken when the stamp was in contact with substrate. **d**, Cross-sectional STEM images of 4, 8, and 15L MoS_2 extracted from design shown in (b), demonstrating atomically-resolved thickness control (all scale bars 10 nm). **e**, Hyperspectral microscope transmission and reflection images near the onset of A-exciton absorption (680 nm), demonstrating uniformly increasing contrast for individual layers. **f**, Absorbance spectra acquired from (a) via hyperspectral microscopy. **g**, Plotted curve fits of excitonic peak positions from optical spectroscopy data (closed symbols PL, open symbols absorbance) with bulk 2H-MoS_2 absorbance peaks extracted from literature[61]. **h**, Photoluminescence spectra of 1-17L MoS_2 acquired from (a).

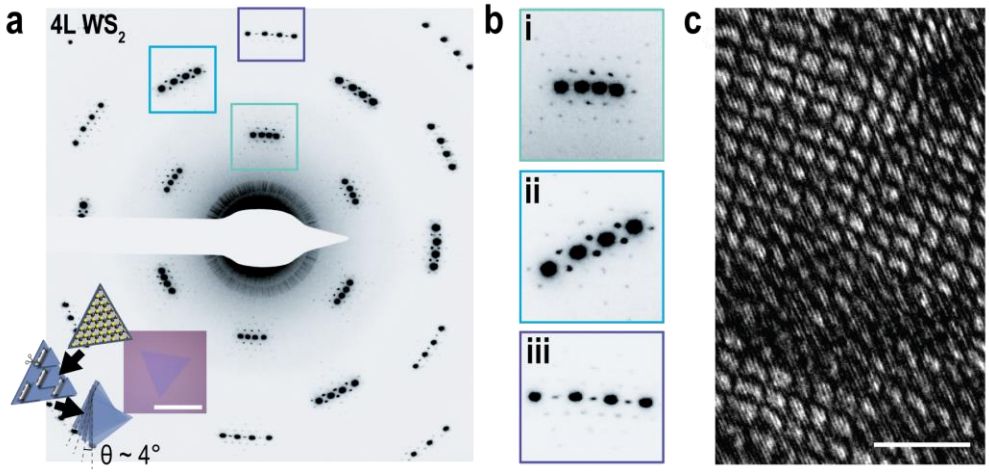

Figure 4. Reconstruction in twisted 4-layer WS_2. a, TEM diffraction pattern acquired from a 4L structure of WS_2 with 4.2° ± 0.2° twist angle between adjacent layers. Inset: Schematic showing method of twisted heterostructure manufacture from single crystal of monolayer WS_2, with optical micrograph of single-crystal WS_2 triangle (scale bar 100 μm). **b**, Magnified views of superlattice peaks for (i) first-, (ii) second-, and (iii) third-order sets of diffraction spots, showing prominent satellite peaks associated with interlayer atomic reconstruction. **c**, A dark-field TEM image with the objective aperture placed over a set of second-order Bragg peaks, showing evidence of atomic reconstruction (scale bar 40 nm) with larger "fishnet" domains attributed to the ~4° twist angle between the innermost layers, and high frequency stripes corresponding to the ~12° twist angle between the outermost layers.

Methods:

Wafer-scale TMDs synthesis.

Monolayer TMDs (MoS_2, WS_2, and WSe_2) were synthesized using MOCVD, as established in prior work[24]. Unless noted otherwise, samples are polycrystalline thin films, composed of complete monolayers or monolayers that are slightly overgrown (having some small bilayer regions nucleated at grain boundaries). Silicon wafers with 300 nm oxide were used as growth substrates. Material was verified to be continuous by atomic force microscopy prior to use.

Template strip lithography (TSL) patterning.

The majority of the TSL patterning in this work used PDMS patterned blocks, with voids as the non-contact regions. The molds for casting PDMS TSL templates were fabricated through standard microfluidics techniques. SU8-3050 photoresist was spun coat on 3 inch silicon wafers, lithographically patterned, hard baked, and silanized with trimethylchlorosilane. PDMS (Sylgard-184) was then poured onto the SU8 molds and cured on a level surface for 2 days at room temperature.

For patterning MOCVD TMDs, a MOCVD growth wafer was first cleaved into ~1 cm^2 chips. A PDMS TSL block was cut to roughly the same size as the chip cleaved for patterning, then gently placed onto the material such that the patterned relief faces towards the material. This structure was exposed to steam for 4-8 seconds, then immediately after, the TSL block was peeled off the chip. After peeling, the pattern transfers to the material. This method is extremely fast and the PDMS molds are reusable. This method was used for the samples in Fig. 1c.i, Fig. 1c.iii, and Fig. 3.

Another method of TSL patterning may employ patterned Au thin films (non-adhesive) embedded in a PMMA thin film. This method was used for the samples shown in Fig. 1c.ii, Fig. 1c.iv, and Fig. 2e.

Our patterning process is as follows: (i) We utilize cleanroom photolithography to produce a flexible, structured template with an atomically-flat bottom surface and spatially patterned regions of strong adhesion. (ii) We apply this adhesive template to the 2D material to achieve uniform contact between the adhesive regions and the sample, then peel the template off. This results in the cleavage and removal of the 2D material within the adhesive regions, leaving behind pixels of patterned material. The pattern in these templates are defined by the non-adhesive regions, voids or inert materials, with negligible adhesion to 2DMs. In principle, the adhesive force can be tuned widely to accommodate various 2D/substrate combinations through the use of different polymers or the addition of intercalant species (e.g., H_2O). TSL samples are imaged under an Olympus BX51 or DSX1000 microscope to confirm high-quality patterning before insertion into the VAR.

Polymer stamp fabrication.

The stamp is carefully designed to modulate substrate-layer-stamp adhesion. Lift rate affects the viscoelastic response of the polymer stamp, which manifests as high adhesion when the stamp is lifted from the substrate quickly or low adhesion when peeled off slowly. Temperature dictates adhesion through polymer reflow when the glass transition is exceeded, or release when the decomposition temperature of the release layer is reached.

The stamp begins as a cylindrical PDMS base (50-800 μm diameter) casted through a similar technique as the TSL patterns. A different PDMS formulation (MasterSil 971-LO) was used due to its low outgassing properties. The subsequent polymer layers were all applied to the casted and cured PDMS by spin coating at 2000 RPM for 1 minute. Optical micrographs of the bottom surface of a poor-quality and high-quality stamp are shown in Supplementary Fig. 4.

Structural integrity was provided by a layer of MicroChem Lift-Off Resist (LOR10B). Its high glass transition temperature (190° C) ensures physical rigidity during the assembly process. This layer improves the surface quality of assembled vdW heterostructures by reducing small-scale surface wrinkles.

The next polymer layer (PCPC-pag) was a polycarbonate derivative dissolved 6 wt% in anisole; additionally, there was 5% of PCPC mass of photoacid generator mixed in. The photoacid compound activates when exposed to either ultraviolet light or elevated temperatures (175° C), thereby initiating degradation of the release layer and physically separating the two surrounding polymer layers.

The final layer was poly(benzyl methacrylate) (PBzMA), dissolved at 6 wt% in anisole. PBzMA has a low glass transition temperature (50° C). The VAR operates above the PBzMA glass transition during heterostructure assembly, allowing this layer to relax into conformal contact when pressed against a targeted vdW material.

Vacuum assembly robot (VAR) system construction.

The vacuum chamber is built from modular components from Ideal Vacuum and the motorized navigation stages are assembled using Newport vacuum-compatible actuators and stages. A 2x - 30x variable magnification microscope looks into the top viewport of the vacuum chamber. The heating stage consists of a vacuum-compatible resistive heater/thermoelectric cooler combination to provide fast and reproducible control over the sample temperature. Control over stage actuation, image acquisition, and system temperature is done through LabView.

General VAR manufacturing process.

Prior to assembly, chips of source material are patterned via TSL and imaged under an Olympus BX51, OLS 5000 LEXT (405 nm laser illumination), or DSX1000 microscope to confirm high-quality patterning before insertion into the VAR.

To initiate patterning, the VAR is equipped with a polymer stamp, chips of patterned material, and a final transfer substrate. Then the system is pumped down to high vacuum. VAR assembly executes as follows:

(1) Translation stage shifts to the user-programmed "pixel" of patterned material.

(2) Imprint platform lowers the polymer stamp towards the targeted pixel as an image processing algorithm runs over the in situ camera view (c.f., Fig. 2c.i and S2).

(3) When the transparent stamp contacts the substrate, change in color contrast is detected and the stamp approach is halted (Supplementary Fig. 3).

(4) Stamp is held in contact with the heated substrate (145° C) for 60 seconds. During the hold period, the polymer adhesion layer relaxes into nanoscale conformal contact. (Optionally) The stage temperature can be lowered to ~T_g of the adhesion or release layers to reduce the deformation upon separation.

(5) Imprint platform rapidly shifts upwards (100 μm at nominally 2000 μm/s) and the material is picked up from the substrate onto the stamp.

This approach-hold-lift loop is executed for all layers programmed into the assembly instruction file. After heterostructure assembly is complete, the vdW solid is delaminated from the stamp onto a final transfer substrate. Various final substrates were used, including native oxide silicon, 300 nm silicon oxide, sapphire, and unpatterned MOCVD TMDs. The VAR executes a different operational protocol for final release:

(1) Stamp is brought into contact with the final substrate at the regular stacking temperature. This minimizes thermal expansion mismatch at the onset of stamp contact.

(2) Translation stage is heated to 175° C to activate the photoacid generator in the release layer (Fig. 2c.ii).

(3) After 5 minutes, the release layer is sufficiently degraded, and the VAR slowly raises the stamp from the substrate (200 nm per second), transferring over the completed heterostructure.

These processes are shown in Supplementary Video 1, at 100x increased speed.

Post-processing manufactured structures.

Completed structures from VAR manufacturing were solvent cleaned (acetone for 45 minutes, or chloroform for 10+ hours) to remove the remnant polymers from the heterostructure surface. Optionally, some were thermally annealed at 300°C for > 6 hours.

Focused ion beam (FIB) 16-tile sample cross-section preparation.

The 16-tile MoS_2 cross-sections were prepared using a Thermo Fisher Helios G4 UX Focused Ion Beam (FIB). The sample chip was positioned such that cross-sections could be cut perpendicular to boundaries between squares of different MoS_2 layer numbers. Protective layers of carbon (~200 nm) and platinum (~1 μm) were deposited on the squares expected to have 4, 8, and 15 MoS_2 layers. Cross-sections were milled from these regions at a 90-degree angle from the sample using a Ga ion beam at 30 kV. The cross-sections were then further polished to electron beam transparency with the ion beam at 5 kV.

Scanning transmission electron microscopy (STEM) 16-tile sample cross-section imaging.

The cross-sections were imaged in a Thermo Scientific Titan Themis STEM at 120 kV with a probe convergence angle of 21.4 mrad. The high-angle annular dark field (HAADF) images show bright bands corresponding to the MoS_2 layers and confirm that the vacuum-assembly technique produced clean stacking and correct layer number in each of the three (4L, 8L, 15L MoS_2) cross-sectional samples. All images were analyzed using the open-source software Cornell Spectrum Imager[62].

Optical photoluminescence, Raman, and hyperspectral transmittance/reflectance microscopy measurements.

The vdW solids were initially transferred via VAR onto a monolayer MOCVD MoS_2 on 300 μm SiO_2/Si substrate. Photoluminescence (PL) of the 16 tile (Fig. 3) was taken on a HORIBA LabRAM HR Evolution Confocal Raman Microscope using a 532 nm laser. A 50x objective was used, which roughly had a 2 μm laser spot size. On the 16-tile structure, a PL map was taken with a *x-y* step size of 12.5 μm so that each tile position had 4 spectra taken, and the monolayer region had 8 spectra taken. Spectra were taken at room temperature under at 0.5mW for 2 acquisitions and 1.2 seconds with a grating of 600 lines/mm. Voigt distributions with a zero background were used to fit the A and B peaks.

For Raman mapping (Supplemental Fig. 11), the MoS_2/WSe_2 heterostructure and monolayer references were illuminated under a 532 nm laser at 0.25 mW. Spectra were acquired using the 100x objective with a grating of 1800 lines/mm. Acquisition time per spectra was 1.5 seconds, resulting in 30-40 minutes for each complete map. A flat noise baseline was subtracted from each individual spectrum, and the integrated area of the respective peaks were used in coloring the Raman map, normalized such that the min/max value for each channel were assigned to min/max color intensity respectively.

For hyperspectral microscopy, the 16-tile structure was transferred onto a 330 μm double-side polished sapphire substrate by first being spin coated with PMMA, then etched in 1M KOH to remove the vdW

solid from the Si, relocated onto water, and controllably water-drain-transferred onto sapphire. The hyperspectral microscope was built with similar specifications to prior work[63], but with slightly modified reflection and transmission objectives for higher resolution. The light source was a Xe bulb and filtered by a monochromator, within a 4 nm spectral resolution. A parallel photodiode was used to monitor the time-dependent Xe signal fluctuation. The photodiode data was used to normalize the signal during separate spectrum acquisitions. The 2D imaging detector was an Andor iXon+ 885 EMCCD.

Both reflection and transmission were taken with the sample facing incident light, meaning the sample had to be flipped over between the two imaging modes. A bare sapphire substrate spectrum was also taken in order to extract this optical constant. Transmission in air without the sample, reflection by a silver mirror, and background signals without illumination were taken as the max transmission, max reflection, and noise level, respectively. Images for each wavelength were first subtracted by the background dark signal, then transformed into transmittance and reflectance by dividing by the max transmission and max reflection images respectively.

Absorption was calculated as:

$$A = -T_0\,(\mathrm{d}T) - R_0\,(\mathrm{d}R)$$

where T_0 is defined as $T_{substrate}/T_{air}$, R_0 is $R_{substrate}/R_{mirror}$, dT is the differential transmission of the sample as $(T_{sample}-T_{substrate})/T_{substrate}$ and dR is the differential reflection as $(R_{sample}-R_{substrate})/R_{substrate}$. The A and B peaks were fit in the 552 nm (2.25 eV) to 708 nm (1.75 eV) range, with a slanted background on two Voigt distributions for the two peaks.

Transfer matrix method calculation of optical response.

The transfer matrix method (TMM) data was calculated using an air-sample-substrate-air system for direct comparison to the experimental data (Supplementary Fig. 12). The sample portion was treated as individual monolayers (e.g. 3L-MoS_2 region in the 16-tile = 1L-MoS_2 + 1L-MoS_2 + 1L-MoS_2).

The optical constant of the 330 micron sapphire substrate was extracted by an inverse-TMM-solver. This showed a minor wavelength dependence due to slight chromatic aberration in the microscope reflectivity at low wavelengths (400-450 nm). The extracted wavelength-dependent sapphire optical constant was then used for the substrate in the *T* and *R* TMM calculation.

2D materials isolated by different methods will display variations in their complex optical constants because of differing synthesis or processing methodologies. Variation in *n* and *k* can be as much as ± 25% comparing the values in currently published work[64–66]. The optical constant used for the MoS_2 for the TMM calculation from published work. We applied a constant prefactor to the *n* and *k* values to calibrate for sample variation between our synthesis and the material used in the reference. The optimal result for matching our monolayer MoS_2 *T* and *R* to that of the published reference came from multiplying *n* by 0.85 and *k* by 0.70. All TMM code was implemented in MATLAB.

Twisted 4L WS_2 fabrication.

Large, randomly oriented single crystals of WS_2 were synthesized via MOCVD on Si/SiO_2 substrates. Growth substrates were cleaved into ~1 cm^2 chips and mounted in the VAR without any TSL patterning. The stamp was used to pick out sub-sections from a large single crystal, with identical numbers of θ-actuator steps taken between layers. The VAR was run in the operator-assisted mode for twisted *N*-layer fabrication. After picking up all layers, the structure was transferred onto a silicon substrate with 300 nm oxide for inspection. Without further post-processing, the final substrate was spun coat with PMMA,

floated in 1M KOH, and transferred onto a 1um holey carbon/copper TEM grid. The TEM grid was then solvent cleaned in acetone to remove all polymer.

Transmission electron microscopy for twisted 4L WS_2.

Dark-field transmission electron microscopy (DF-TEM) and selected area electron diffraction (SAED) of the twisted 4 layer WS_2 sample were performed on TFS Talos (operated at 200 keV) equipped with Gatan OneView Camera. DF-TEM images were formed by placing an objective aperture around the optic axis and tilting beam to achieve two-beam conditions around diffraction peaks of interest.

Thin film sample preparation

Au thin films 20 nm thick were deposited in an AJA-Orion 8E electron beam evaporation system onto native oxide-coated Si wafers.

Exfoliated Sample Preparation and Cryogenic photoluminescence measurements.

Exfoliated flakes of kish graphite and hBN, were deposited onto Si/SiO_2 substrates. For the cryogenic experiments, source flakes (hBN from HQGraphene; WSe_2 from 2D Semiconductors) were exfoliated onto Si/SiO_2 substrates. The source flakes were inserted into the VAR and an hBN/WSe_2/hBN stack was fabricated. The sample was subsequently cleaned of polymer residue via solvent washing and thermal annealing and inserted into a closed cycle optical cryostat for measurement at 7 K. For the PL measurements, we excite the sample above band gap with a diffraction-limited 518 nm pump with power ~2 μW. For the differential reflectivity measurements, we utilize a broadband LED light source to measure $dR = R_{WSe2} / R_{hBN} - 1$, where R_{WSe2} (R_{hBN}) is the reflection from the heterostructure collected within (outside) the monolayer region.

Confocal Laser Scanning Microscopy

An Olympus OLS 5000 LEXT was used to acquire the images for confocal laser scanning microscopy in Supplementary Fig. 10. The 20x objective was used for the low magnification white light image and the 100x objective was used for the high magnification white light image and confocal intensity image. The brightness setting was kept constant for the intensity images. (30 by 30) μm^2 square ROIs centered in the middle of each intensity image was used to create the histograms for the plot in Supplementary Fig. 10d.

Acknowledgements:

Primary funding for this work comes from the National Science Foundation through Platform for the Accelerated Realization, Analysis, and Discovery of Interface Materials (PARADIM) under Cooperative Agreement No. DMR-2039380 and the University of Chicago MRSEC (DMR-2011854). It was partially supported by Air Force Office of Scientific Research MURI project (FA9550-18-1-0480). Materials growths done by C.P. are partially supported by Samsung Advanced Institute of Technology. This work made use of the shared facilities at the University of Chicago Materials Research Science and Engineering Center, supported by National Science Foundation under award number DMR-2011854. This work made use of the Pritzker Nanofabrication Facility, which receives partial support from the SHyNE Resource, a node of the National Science Foundation's National Nanotechnology Coordinated Infrastructure (NSF ECCS-2025633), and the Searle Cleanroom which was procured with funding generously provided by The Searle Funds at The Chicago Community Trust (Grant A2010-03222). A.J.M. was supported by the Kadanoff-Rice Postdoctoral Fellowship of the UChicago MRSEC, DMR-2011854. A.Y. is supported by the Department of Defense (DoD) through the National Defense Science & Engineering Graduate (NDSEG) Fellowship Program. A.R. and electron microscopy at the Cornell Center for Materials Research are supported by the NSF-MRSEC grant DMR-1719875. The Titan microscope at Cornell was acquired with the NSF MRI grant DMR-1429155. This work made use of the Michigan Center for Materials Characterization. R.H. acknowledges support from W.M. Keck Foundation. S.H.S. acknowledges support from the Army Research Office (W911NF-17-S-0002).

Author Contributions:

A.J.M. and J.P. conceived the main ideas of this work. A.J.M. and A.Y. built the VAR, designed the polymer stamps. C.P. and A.J.M. formulated the TSL patterning technique. A.Y., F.M., C.P., and J.K. grew the MOCVD TMDs materials used in this work. A.Y. and A.J.M. performed the VAR manufacturing of the presented vdW solids. A.Y. and M.L. acquired and analyzed the optical measurements. A.Y. wrote the code and analyzed the results from the TMM optical calculations and

performed the LCSM and Raman mapping measurements. A.R. took the FIB cross-section and STEM data. S.H.S. took the SAED and DF-TEM of the twisted 4L WS_2 structure, and performed the multislice simulation of the rigid twisted 4L WS_2 structure. A.Y. and R.S. fabricated the exfoliated samples for which R.S. measured cryogenic optical response. A.H. and R.S. analyzed and discussed the cryogenic measurements on the exfoliated heterostructure. D.A.M., and R.H. aided in discussion and interpretation of the STEM and TEM data. A.J.M., A.Y., and J.P. wrote the paper, with input from all coauthors.

References

1. Geim, A. K. & Grigorieva, I. V. Van der Waals heterostructures. *Nature* **499**, 419–425 (2013).
2. Song, J. C. W. & Gabor, N. M. Electron quantum metamaterials in van der Waals heterostructures. *Nat. Nanotechnol.* **13**, 986–993 (2018).
3. Cao, Y. *et al.* Unconventional superconductivity in magic-angle graphene superlattices. *Nature* **556**, 43–50 (2018).
4. Lu, X. *et al.* Superconductors, orbital magnets and correlated states in magic-angle bilayer graphene. *Nature* **574**, 653–657 (2019).
5. Balents, L., Dean, C. R., Efetov, D. K. & Young, A. F. Superconductivity and strong correlations in moiré flat bands. *Nat. Phys.* **16**, 725–733 (2020).
6. Rivera, P. *et al.* Interlayer valley excitons in heterobilayers of transition metal dichalcogenides. *Nat. Nanotechnol.* **13**, 1004–1015 (2018).
7. Sung, J. *et al.* Broken mirror symmetry in excitonic response of reconstructed domains in twisted $MoSe_2$/$MoSe_2$ bilayers. *Nat. Nanotechnol.* **15**, 750–754 (2020).
8. Brotons-Gisbert, M. *et al.* Spin–layer locking of interlayer excitons trapped in moiré potentials. *Nat. Mater.* **19**, 630–636 (2020).
9. Jin, C. *et al.* Observation of moiré excitons in WSe_2/WS_2 heterostructure superlattices. *Nature* **567**, 76–80 (2019).
10. Tran, K. *et al.* Evidence for moiré excitons in van der Waals heterostructures. *Nature* **567**, 71–75 (2019).
11. Alexeev, E. M. *et al.* Resonantly hybridized excitons in moiré superlattices in van der Waals heterostructures. *Nature* **567**, 81–86 (2019).

12. Shimazaki, Y. *et al.* Strongly correlated electrons and hybrid excitons in a moiré heterostructure. *Nature* **580**, 472–477 (2020).
13. Xu, Y. *et al.* Correlated insulating states at fractional fillings of moiré superlattices. *Nature* **587**, 214–218 (2020).
14. Tang, Y. *et al.* Simulation of Hubbard model physics in WSe_2/WS_2 moiré superlattices. *Nature* **579**, 353–358 (2020).
15. Xie, Y. *et al.* Spectroscopic signatures of many-body correlations in magic-angle twisted bilayer graphene. *Nature* **572**, 101–105 (2019).
16. Kim, K. *et al.* van der Waals heterostructures with high accuracy rotational alignment. *Nano Lett.* **16**, 1989–1995 (2016).
17. Liu, Y., Huang, Y. & Duan, X. Van der Waals integration before and beyond two-dimensional materials. *Nature* **567**, 323–333 (2019).
18. Akinwande, D. *et al.* Graphene and two-dimensional materials for silicon technology. *Nature* **573**, 507–518 (2019).
19. Sharpe, A. L. *et al.* Emergent ferromagnetism near three-quarters filling in twisted bilayer graphene. *Science* **365**, 605–608 (2019).
20. Wang, L. *et al.* Correlated electronic phases in twisted bilayer transition metal dichalcogenides. *Nat. Mater.* **19**, 861–866 (2020).
21. Park, J. M., Cao, Y., Watanabe, K., Taniguchi, T. & Jarillo-Herrero, P. Tunable strongly coupled superconductivity in magic-angle twisted trilayer graphene. *Nature* **590**, 249–255 (2021).
22. Banszerus, L. *et al.* Ultrahigh-mobility graphene devices from chemical vapor deposition on reusable copper. *Science Advances* **1**, e1500222 (2015).
23. Zhang, J. *et al.* New Growth Frontier: Superclean Graphene. *ACS Nano* **14**, 10796–10803 (2020).
24. Kang, K. *et al.* High-mobility three-atom-thick semiconducting films with wafer-scale homogeneity. *Nature* **520**, 656–660 (2015).
25. Xu, X. *et al.* Seeded 2D epitaxy of large-area single-crystal films of the van der Waals

semiconductor 2H $MoTe_2$. *Science* **372**, 195–200 (2021).

26. Masubuchi, S. *et al.* Autonomous robotic searching and assembly of two-dimensional crystals to build van der Waals superlattices. *Nat. Commun.* **9**, 1413 (2018).
27. Pizzocchero, F. *et al.* The hot pick-up technique for batch assembly of van der Waals heterostructures. *Nat. Commun.* **7**, 11894 (2016).
28. Fritz, N., Dao, H., Allen, S. A. B. & Kohl, P. A. Polycarbonates as temporary adhesives. *Int. J. Adhes. Adhes.* **38**, 45–49 (2012).
29. Castellanos-Gomez, A. *et al.* Deterministic transfer of two-dimensional materials by all-dry viscoelastic stamping. *2D Mater.* **1**, 011002 (2014).
30. Liu, Y. *et al.* Approaching the Schottky–Mott limit in van der Waals metal–semiconductor junctions. *Nature* **557**, 696–700 (2018).
31. Went, C. M. *et al.* A new metal transfer process for van der Waals contacts to vertical Schottky-junction transition metal dichalcogenide photovoltaics. *Science Advances* **5**, eaax6061 (2019).
32. Kum, H. S. *et al.* Heterogeneous integration of single-crystalline complex-oxide membranes. *Nature* **578**, 75–81 (2020).
33. Zhong, Y. *et al.* Wafer-scale synthesis of monolayer two-dimensional porphyrin polymers for hybrid superlattices. *Science* **366**, 1379–1384 (2019).
34. Lin, Y.-C. *et al.* Graphene annealing: how clean can it be? *Nano Lett.* **12**, 414–419 (2012).
35. Wood, J. D. *et al.* Annealing free, clean graphene transfer using alternative polymer scaffolds. *Nanotechnology* **26**, 055302 (2015).
36. Nagpal, P., Lindquist, N. C., Oh, S.-H. & Norris, D. J. Ultrasmooth patterned metals for plasmonics and metamaterials. *Science* **325**, 594–597 (2009).
37. Hsu, C. *et al.* Thickness-Dependent Refractive Index of 1L, 2L, and 3L MoS_2, $MoSe_2$, WS_2, and WSe_2. *Advanced Optical Materials* **7**, 1900239 (2019).
38. Morozov, Y. V. & Kuno, M. Optical constants and dynamic conductivities of single layer MoS_2, $MoSe_2$, and WSe_2. *Applied Physics Letters* **107**, 083103 (2015).

39. Song, B. *et al.* Complex Optical Conductivity of Two-Dimensional MoS_2: A Striking Layer Dependency. *J. Phys. Chem. Lett.* **10**, 6246–6252 (2019).
40. Ji, H. G., Solís-Fernández, P., Erkılıç, U. & Ago, H. Stacking orientation-dependent photoluminescence pathways in artificially stacked bilayer WS_2 nanosheets grown by chemical vapor deposition: implications for spintronics and valleytronics. *ACS Applied Nano Materials* **4**, 3717–3724 (2021).
41. Niu, Y. *et al.* Thickness-Dependent Differential Reflectance Spectra of Monolayer and Few-Layer MoS_2, $MoSe_2$, WS_2 and WSe_2. *Nanomaterials* **8**, (2018).
42. Morozov, Y. V. & Kuno, M. Optical constants and dynamic conductivities of single layer MoS_2, $MoSe_2$, and WSe_2. *Applied Physics Letters* **107**, 083103 (2015).
43. Havener, R. W. *et al.* Hyperspectral imaging of structure and composition in atomically thin heterostructures. *Nano Lett.* **13**, 3942–3946 (2013).
44. Huang, S. *et al.* Probing the interlayer coupling of twisted bilayer MoS_2 using photoluminescence spectroscopy. *Nano Lett.* **14**, 5500–5508 (2014).
45. Liu, K. *et al.* Evolution of interlayer coupling in twisted molybdenum disulfide bilayers. *Nat. Commun.* **5**, 4966 (2014).
46. Mak, K. F., Lee, C., Hone, J., Shan, J. & Heinz, T. F. Atomically thin MoS_2: a new direct-gap semiconductor. *Phys. Rev. Lett.* **105**, 136805 (2010).
47. Cho, Y. & Berkelbach, T. C. Environmentally sensitive theory of electronic and optical transitions in atomically thin semiconductors. *Phys. Rev. B Condens. Matter* **97**, 041409 (2018).
48. Raja, A. *et al.* Dielectric disorder in two-dimensional materials. *Nat. Nanotechnol.* **14**, 832–837 (2019).
49. Ugeda, M. M. *et al.* Giant bandgap renormalization and excitonic effects in a monolayer transition metal dichalcogenide semiconductor. *Nat. Mater.* **13**, 1091–1095 (2014).
50. Chubarov, M. *et al.* Wafer-Scale Epitaxial Growth of Unidirectional WS2 Monolayers on Sapphire. *ACS Nano* **15**, 2532–2541 (2021).

51. Liao, M. *et al.* Precise control of the interlayer twist angle in large scale MoS2 homostructures. *Nat. Commun.* **11**, 2153 (2020).
52. Yoo, H. *et al.* Atomic and electronic reconstruction at the van der Waals interface in twisted bilayer graphene. *Nat. Mater.* **18**, 448–453 (2019).
53. Weston, A. *et al.* Atomic reconstruction in twisted bilayers of transition metal dichalcogenides. *Nat. Nanotechnol.* **15**, 1–6 (2020).
54. Quan, J. *et al.* Phonon renormalization in reconstructed MoS_2 moiré superlattices. *Nat. Mater.* 1–6 (2021).
55. Kim, C.-J. *et al.* Chiral atomically thin films. *Nat. Nanotechnol.* **11**, nnano.2016.3 (2016).
56. Scuri, G. *et al.* Electrically Tunable Valley Dynamics in Twisted WSe_{2}/WSe_{2} Bilayers. *Phys. Rev. Lett.* **124**, 217403 (2020).
57. Yao, K. *et al.* Enhanced tunable second harmonic generation from twistable interfaces and vertical superlattices in boron nitride homostructures. *Sci Adv* **7**, (2021).
58. Shen, C. *et al.* Correlated states in twisted double bilayer graphene. *Nat. Phys.* **16**, 520–525 (2020).
59. He, M. *et al.* Symmetry breaking in twisted double bilayer graphene. *Nat. Phys.* **17**, 26–30 (2020).
60. Lu, D. *et al.* Synthesis of freestanding single-crystal perovskite films and heterostructures by etching of sacrificial water-soluble layers. *Nat. Mater.* **15**, 1255–1260 (2016).
61. Morozov, Y. V. & Kuno, M. Optical constants and dynamic conductivities of single layer MoS_2, $MoSe_2$, and WSe_2. *Applied Physics Letters* **107**, 083103 (2015).
62. Cueva, P., Hovden, R., Mundy, J. A., Xin, H. L. & Muller, D. A. Data processing for atomic resolution electron energy loss spectroscopy. *Microsc. Microanal.* **18**, 667–675 (2012).
63. Havener, R. W. *et al.* Hyperspectral imaging of structure and composition in atomically thin heterostructures. *Nano Lett.* **13**, 3942–3946 (2013).
64. Zhang, H. *et al.* Measuring the refractive index of highly crystalline monolayer MoS2 with high confidence. *Sci. Rep.* **5**, 8440 (2015).
65. Liu, H.-L. *et al.* Temperature-dependent optical constants of monolayer MoS_2, $MoSe_2$, WS_2, and

WSe_2: spectroscopic ellipsometry and first-principles calculations. *Sci. Rep.* **10**, 15282 (2020).

66. Jung, G.-H., Yoo, S. & Park, Q.-H. Measuring the optical permittivity of two-dimensional materials without a priori knowledge of electronic transitions. *Nanophotonics* **8**, 263–270 (2018).